Space Object Shape Characterization and Tracking Using Light Curve and Angles Data

Richard Linares*

University at Buffalo, State University of New York, Amherst, NY, 14260-4400

Moriba K. Jah†

Air Force Research Laboratory, Kirtland AFB, New Mexico, 87117

John L. Crassidis‡, Christopher K. Nebelecky§

University at Buffalo, State University of New York, Amherst, NY, 14260-4400

This paper presents a new method, based on a multiple-model adaptive estimation approach, to determine the most probable shape of a resident space object among a number of candidate shape models while simultaneously recovering the observed resident space object's inertial orientation and trajectory. Multiple-model adaptive estimation uses a parallel bank of filters, each operating under a different hypothesis to determine an estimate of the physical system under consideration. In this work, the shape model of the resident space object constitutes the hypothesis. Estimates of the likelihood of each hypothesis given the available measurements are provided from the multiple-model adaptive estimation approach. The multiple-model adaptive estimation state estimates are determined using a weighted average of the individual filter estimates, whereas the shape estimate is selected as the shape model with the highest likelihood. Each filter employs the Unscented estimation approach, reducing passively-collected electro-optical data to infer the unknown state vector comprised of the resident

*Graduate Student, Department of Mechanical & Aerospace Engineering. Email: linares2@buffalo.edu. Student Member AIAA.

†Senior Aerospace Engineer. Associate Fellow AIAA.

‡Professor, Department of Mechanical & Aerospace Engineering. Email: johnc@buffalo.edu, Associate Fellow AIAA.

§Graduate Student, Department of Mechanical & Aerospace Engineering. Email: ckn@buffalo.edu. Student Member AIAA.

space object's inertial-to-body orientation, position and respective temporal rates. Each hypothesized shape model results in a different observed optical cross-sectional area. The effects of solar radiation pressure may be recovered from accurate angles-data alone, if the collected measurements span a sufficiently long period of time, so as to make the non-conservative mismodeling effects noticeable. However, for relatively short arcs of data, this effect is weak and thus the temporal brightness of the resident space object can be used in conjunction with the angles data to exploit the fused sensitivity to both resident space object shape model and associated trajectory. Initial simulation results show that the resident space object model and states can be recovered accurately with the proposed approach.

I. Introduction

In recent years space situational awareness, which is concerned with collecting and maintaining knowledge of all objects orbiting the Earth, has gained much attention. The U.S. Air Force collects the necessary data for space object catalog development and maintenance through a global network of radar and optical sensors. Due to the fact that a limited number of sensors are available to track a large number of resident space objects (RSOs), the sparse data collected must be exploited to the fullest extent. Various sensors, such as radar, exist for RSO state estimation; typically position, velocity, and a non-conservative force parameter B^* analogous to a ballistic coefficient. Another piece of useful information is the estimation of the shape of an RSO. When considering the shape of an RSO, the orientation (attitude) becomes a quantity of interest.

Shape estimation is an important issue in the observation of RSOs since the shape influences the dynamics of the object and may provide valuable information on the object's origin or intent. There exists a number of methods for estimating the shape of an object. For example, radar-based methods have been extensively used for shape estimation, which include radar cross-sectioning approaches[1] and range Doppler interferometry.[2] These techniques were first developed in the field of planetary radar astronomy to estimate the shape of natural satellites,[3] but were later applied to the imaging of artificial Earth orbiting satellites. In low-Earth orbit, some RSOs can be imaged but these methods are limited by the RSO size and distance.[4]

Laser radar-based (LADAR) methods have also been used to estimate the shape of RSOs. LADAR provides a three-dimensional scan of the object, returning a cloud of points of the measured relative position of an object. Although LADAR measurements can provide very detailed shape information, due to range limitations, they are only effective for rendezvous and proximity operations. Reference 5 uses LADAR scans to perform a least squares fit of

the LADAR returns to previously assembled point cloud models to estimate the shape of an RSO. Reference 6 developes a filter approach to simultaneously estimate dynamic states, geometric shape, and mass model parameters of a satellite using multiple observations with LADAR sensors. In Ref. 6 a probabilistic map of the RSO is constructed using a sensor uncertainty model and the dynamics experienced by the RSO to estimate its shape.

Resolved imaging methods have also have been used to estimate the size and shape of RSOs.[7] These methods work either directly with the pixels of the images or are used to identify features of the RSO. Features, such as corners, edges and markers, are located and tracked temporally to estimate higher level motion and the structure of the rigid body.[8] The feature-based methods rely on continuously identifying and tracking higher level traits of the RSO through the use of a Kalman filter to estimate feature location and motion parameters. Although these methods estimate the motion of features they do not by themselves provide a detailed estimate of the shape of the object, but rather only the location of a sparse set of feature points on the object. Pixel-based methods rely on pixel-level information, and use the shading, texture and optical flow of the images to estimate the shape of an object at each time step using a monocular camera. Since these methods rely on pixel-level computations, they typically involve very high-dimensional states and therefore are very computationally expensive. These methods are also very sensitive to pixel-level detail and are easily corrupted by unpredictable light intensities caused by surface irregularities. Because of the high resolution required to resolve meaningful shape estimates, pixel-based methods are only effective for space-based sensors and/or high resolution ground-based telescopes.

Some powerful ground-based telescopes, such as the Air Force Maui Optical and Supercomputing site Advanced Electro-Optical System, can resolve RSOs such as the Hubble Space Telescope and the International Space Station to very high detail, but most objects are too small and/or too distant to lend themselves to ground-based resolved imaging.[4] For example, operational RSOs in geosynchronous orbits, micro- and nanosatellites cannot be resolved using ground-based optical observations. Angular measurements of these objects are still made to estimate their orbits. The angular measurements are made by collecting light reflected off the RSO with an optical sensor. Although the amount of light collected from these objects is limited, information can still be extracted which can be used to estimate the RSOs shape.

Light curves, the temporal brightness of an observed RSO, have been exploited for shape estimation. Light curve approaches have been studied to estimate the shape and state of asteroids.[9,10] Reference 11 uses light curve and thermal emissions to recover the three-dimensional shape of an object assuming its orientation with respect to the observer is known. The benefits of using a light curve-based approach over the aforementioned others is that it is not limited to large objects in lower orbits; it can be applied to small and/or dim objects

in higher orbits, such as geosynchronous. In this paper, light curve data is considered for shape estimation, which is useful because it provides a mechanism to estimate both position and attitude, as well as their respective rates.[12,13]

Several aspects of using light curve data make it particularly advantageous for object detection, identification, characterization and tracking. Light curve data is the time-varying sensor wavelength-dependent apparent magnitude of energy (i.e. photons) scattered (reflected) off of an object along the line-of-sight to an observer. Because the apparent magnitude of an RSO is a function of its size, orientation, and surface material properties, one or more of these characteristics should be recoverable. This can aid in the detection and identification of an RSO after a catalog of spacecraft data with material properties is developed, and may also prove to be powerful for never-seen-before objects.

There is a coupling between RSO attitude and non-conservative accelerations. This can be exploited to assist in the estimation of the RSO trajectory. Likewise, the measurement of the apparent magnitude is a function of several RSO characteristics. These same characteristics drive certain non-conservative forces, such as the acceleration caused by solar radiation pressure (SRP). The acceleration due to SRP is modeled as function of an object's Sun-facing area and surface properties. It has a very small magnitude compared to gravitational accelerations, and typically has an order of magnitude around 10^{-7} to 10^{-9} km/s^2, but is the dominant non-conservative acceleration for objects above 1,000 km. Below 1,000 km, atmospheric drag is the dominating non-conservative acceleration.

Filtering algorithms for state estimation, such as the extended Kalman filter (EKF),[14] the Unscented Kalman filter (UKF)[15] and particle filters[16] are commonly used to both estimate hidden (indirectly observable) states and filter noisy measurements. The basic difference between the EKF and the UKF results from the manner in which the state distribution of the nonlinear models is approximated. The UKF, introduced by Julier and Uhlmann,[15] uses a nonlinear transformation called the unscented transform, in which the state probability density function (pdf) is represented by a set of weighted sigma points. When the sigma points are propagated through the nonlinear system, the posterior mean and covariance are obtained up to the second order for any nonlinearity. Both the EKF and UKF assume that the process noise term is represented by a zero-mean Gaussian white-noise process and that the measurement noise is modeled as a zero-mean Gaussian random variable. Furthermore both approaches assume that the *a posteriori* pdf is Gaussian in a linear domain. This is true given the previous assumptions but under the effect of nonlinear measurement functions and system dynamics the initial Gaussian state uncertainty may quickly become non-Gaussian. Both filters only provide approximate solutions to the nonlinear filtering problem, since the *a posteriori* pdf is in general non-Gaussian due to nonlinear effects. The EKF typically works well only in the region where the first-order Taylor-series linearization adequately approxi-

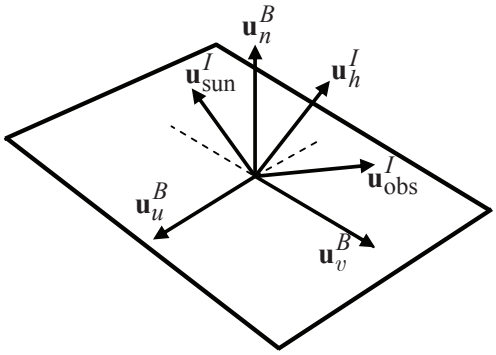

Figure 1. Geometry of Reflection

mates the non-Gaussian pdf. The UKF provides higher-order moments for the computation of the *a posteriori* pdf without the need to calculate Jacobian matrices as required in the EKF. In this work, the UKF is used as the mechanism for state estimation because the light curve observation model is highly nonlinear and Jacobian calculations are non-trivial.

Attitude estimation using light curve data has been demonstrated in Ref. 17. The main goal of the present work is to use light curve data to, autonomously and in near realtime, estimate the shape of an RSO along with its rotational (including attitude) and translational states. This is accomplished by means of a multiple-model adaptive estimation (MMAE) approach. For the MMAE approach, the hypotheses tested are different candidate RSO shape models. By computing the likelihood associated with each hypothesis, the MMAE determines which of the candidate shape models is most probable given the observations. The MMAE state estimate is given by the weighted average of each filter's estimate. The weights correspond to the normalized likelihood derived from Bayes' rule using the unknown states conditioned on the current-time measurement residual and innovations covariance.

The organization of this paper is as follows. First, the models for RSO shape, orbital dynamics, and attitude dynamics are discussed. Then a description of the measurement models used in this paper are given. Next, a review of the UKF approach is provided. Following this, the MMAE structure is outlined and discussed. Finally, simulation results of the shape estimation approach are provided.

II. Shape Model Definition

The shape models considered in this work consist of a finite number a flat facets. For curved surfaces the model become more accurate as the number of facets are increased. Each facet has a set of three orthogonal basis vectors, $\{\mathbf{u}_n^B,\ \mathbf{u}_u^B,\ \mathbf{u}_v^B\}$, associated with it as defined in Figure 1. The unit vector $\mathbf{u}_n^B$ points in the direction of the outward normal of the facet and the vectors $\mathbf{u}_u^B$ and $\mathbf{u}_v^B$ lay in the plane of the facet. The notation superscript B denotes

that the vector is expressed in body coordinates. For this study, the resident space objects (RSOs) are assumed to be rigid bodies and therefore the unit vectors $\mathbf{u}_n^B$, $\mathbf{u}_u^B$ and $\mathbf{u}_v^B$ do not change over time.

The light curve and the solar radiation pressure models discussed in subsequent sections require that some of the body vectors be expressed in inertial coordinates. Vectors expressed in body coordinates can be rotated to the inertial frame via

$$\mathbf{u}_k^B = A(\mathbf{q}_I^B)\ \mathbf{u}_k^I, \quad k = u,\, v,\, n \tag{1}$$

where $A(\mathbf{q}_I^B)$ is the attitude matrix mapping the inertial frame to the body frame using the quaternion parameterization. The superscript I denotes that a vector is expressed in inertial coordinates. The vector $\mathbf{u}_{\text{sun}}^I$ is a unit vector pointing from the RSO to the Sun and the unit vector $\mathbf{u}_{\text{obs}}^I$ points from the RSO to the observer. The vector $\mathbf{u}_h^I$ is the normalized half vector between $\mathbf{u}_{\text{sun}}^I$ and $\mathbf{u}_{\text{obs}}^I$; this vector is also known as the Sun-RSO-Observer bisector. Each facet has an area $\mathcal{A}(i)$ associated with it, where i is the facet identifier. Once the number of facets, N, has been defined, the basis vectors $\{\mathbf{u}_n^B(i),\ \mathbf{u}_u^B(i),\ \mathbf{u}_v^B(i)\}$ and areas $\mathcal{A}(i)$ define the size and shape of the RSO.

III. System Models

A. Orbital and Attitude System Model

In this paper the inertial position and velocity of an Earth orbiting RSO are denoted by $\mathbf{r}^I = [x \quad y \quad z]^T$ and $\mathbf{v}^I = [v_x \quad v_y \quad v_z]^T$, respectively. For this work, the equations of motion of the RSO are modeled by

$$\ddot{\mathbf{r}}^I = -\frac{\mu}{r^3}\mathbf{r}^I + \mathbf{a}_{J_2} + \mathbf{a}_{\text{srp}}^I \tag{2}$$

where μ is the Earth's gravitational parameter, $r = \|\mathbf{r}^I\|$, $\mathbf{a}_{J_2}$ is the gravitational perturbation due to non-symmetric distribution of mass along the lines of latitude and $\mathbf{a}_{\text{srp}}^I$ represents the acceleration perturbation due to SRP, which will be discussed in detail in the following section. The acceleration due to the J_2 effect is given by

$$\mathbf{a}_{J_2} = -\frac{3}{2}J_2\left(\frac{\mu}{r^2}\right)\left(\frac{R_\oplus}{r}\right)^2\begin{bmatrix}\left(1-5\left(\frac{z}{r}\right)^2\right)\frac{x}{r}\\ \left(1-5\left(\frac{z}{r}\right)^2\right)\frac{y}{r}\\ \left(3-5\left(\frac{z}{r}\right)^2\right)\frac{z}{r}\end{bmatrix} \tag{3}$$

where $J_2 = 1.082\ 626\ 683\ \times 10^{-3}$ is the coefficient for the second zonal harmonic and $R_\oplus = 6,378.137$ km is the mean equatorial radius of the Earth.

A number of parameterizations exist to specify attitude, including Euler angles, quaternions, and Rodrigues parameters.[18] This paper uses the quaternion, which is based on the Euler angle/axis parametrization. The quaternion is defined as $\mathbf{q} \equiv [\boldsymbol{\varrho}^T \quad q_4]^T$ with $\boldsymbol{\varrho} = \hat{\mathbf{e}} \sin(\nu/2)$, and $q_4 = \cos(\nu/2)$, where $\hat{\mathbf{e}}$ and ν are the Euler axis of rotation and rotation angle, respectively. Clearly, the quaternion must satisfy a unit norm constraint, $\mathbf{q}^T\mathbf{q} = 1$. In terms of the quaternion, the attitude matrix is given by

$$A(\mathbf{q}) = \Xi^T(\mathbf{q})\Psi(\mathbf{q}) \tag{4}$$

where

$$\Xi(\mathbf{q}) \equiv \begin{bmatrix} q_4 I_{3\times 3} + [\boldsymbol{\varrho}\times] \\ -\boldsymbol{\varrho}^T \end{bmatrix} \tag{5a}$$

$$\Psi(\mathbf{q}) \equiv \begin{bmatrix} q_4 I_{3\times 3} - [\boldsymbol{\varrho}\times] \\ -\boldsymbol{\varrho}^T \end{bmatrix} \tag{5b}$$

with

$$[\mathbf{g}\times] \equiv \begin{bmatrix} 0 & -g_3 & g_2 \\ g_3 & 0 & -g_1 \\ -g_2 & g_1 & 0 \end{bmatrix} \tag{6}$$

for any general 3×1 vector $\mathbf{g}$ defined such that $[\mathbf{g}\times]\mathbf{b} = \mathbf{g} \times \mathbf{b}$.

The rotational dynamics are given by the coupled first order differential equations:

$$\dot{\mathbf{q}}_I^B = \frac{1}{2}\Xi(\mathbf{q}_I^B)\boldsymbol{\omega}_{B/I}^B \tag{7a}$$

$$\dot{\boldsymbol{\omega}}_{B/I}^B = J_{\text{RSO}}^{-1}\left(\mathbf{T}_{\text{srp}}^B - \left[\boldsymbol{\omega}_{B/I}^B\times\right] J_{\text{RSO}}\boldsymbol{\omega}_{B/I}^B\right) \tag{7b}$$

where $\boldsymbol{\omega}_{B/I}^B$ is the angular velocity of the RSO with respect to the inertial frame, expressed in body coordinates, J_{RSO} is the inertia matrix of the RSO and $\mathbf{T}_{\text{srp}}^B$ is the net torque acting on the RSO due to SRP, expressed in body coordinates.

B. Solar Radiation Pressure Model

For higher altitude objects ($\geq$ 1,000 km), SRP represents the primary non-conservative perturbation acting on RSOs. Because SRP depends upon the RSO's position and orientation, its effect couples the position and attitude dynamics.

For an RSO comprised of a collection of N facets as defined in Figure 1, the acceleration perturbation due to SRP is given by[19,20]

$$\mathbf{a}_{\text{srp}}^{I} = \sum_{i=1}^{N} \mathbf{a}_{\text{srp}}^{I}(i) \tag{8a}$$

$$\mathbf{a}_{\text{srp}}^{I}(i) = \frac{-S_F \mathcal{A}(i) \cos^2(\psi(i))\, G[\cos(\psi(i))]}{m_{\text{RSO}}\ c\ d^2} \mathbf{u}_{\text{srp}}^{I}(i) \tag{8b}$$

$$\mathbf{u}_{\text{srp}}^{I}(i) = 2\left[\frac{R_{\text{diff}}(i)}{3} + \frac{R_{\text{abs}}(i)\epsilon(i)}{3} + R_{\text{spec}}(i)\cos(\psi(i))\right]\mathbf{u}_{n}^{I}(i) + [1 - R_{\text{spec}}(i)]\mathbf{u}_{\text{sun}}^{I} \tag{8c}$$

where $S_F = 1,367$ W/m^2 is referred to as the solar-radiation constant and is a measure of the flux density of electromagnetic radiation incident on a sphere of radius 1 AU centered at the Sun, $c = 299,792,458$ m/s is the speed of light in a vacuum, d is the distance between the RSO and the Sun expressed in AU, m_{RSO} is the mass of the RSO, $\epsilon(i)$, $\mathcal{A}(i)$ and $\mathbf{u}_n^I(i)$ are the emissivity, total area and normal vector for the i^{th} facet, respectively, and $R_{\text{spec}}(i)$, $R_{\text{diff}}(i)$ and $R_{\text{abs}}(i)$ are the spectral reflectance, diffuse reflectance and absorption coefficients, respectively, which are assumed constant over the entire facet. Under the assumption that no energy is transmitted through the facet it follows that

$$R_{\text{spec}}(i) + R_{\text{diff}}(i) + R_{\text{abs}}(i) = 1 \tag{9}$$

In addition, $\cos(\psi(i)) \equiv \mathbf{u}_n^I(i) \cdot \mathbf{u}_{\text{sun}}^I$ is the cosine of the inclination of the i^{th} facet towards the Sun. The function $G[a] \equiv \max[0, \text{sign}(a)]$ will be zero when a facet is shaded from the Sun (i.e. $\cos(\psi(i)) \leq 0$) and one when the facet is illuminated.

Equation (8b) can also be used to determine the torque on the RSO due to SRP. Because the spectral reflectance, diffuse reflectance and absorption coefficients are constant over the entire facet, the contribution of SRP over the entire facet can be assumed to be a single force acting on the centroid of the facet. The total torque is then given by

$$\mathbf{T}_{\text{srp}}^{B} = m_{\text{RSO}} \sum_{i=1}^{N} \left[\boldsymbol{\ell}^{B}(i)\times\right]\left(A(\mathbf{q}_I^B)\mathbf{a}_{\text{srp}}^{I}(i)\right) \tag{10}$$

where $\boldsymbol{\ell}^B(i)$ is the position vector from the center of mass of the RSO to the centroid of i^{th} facet.

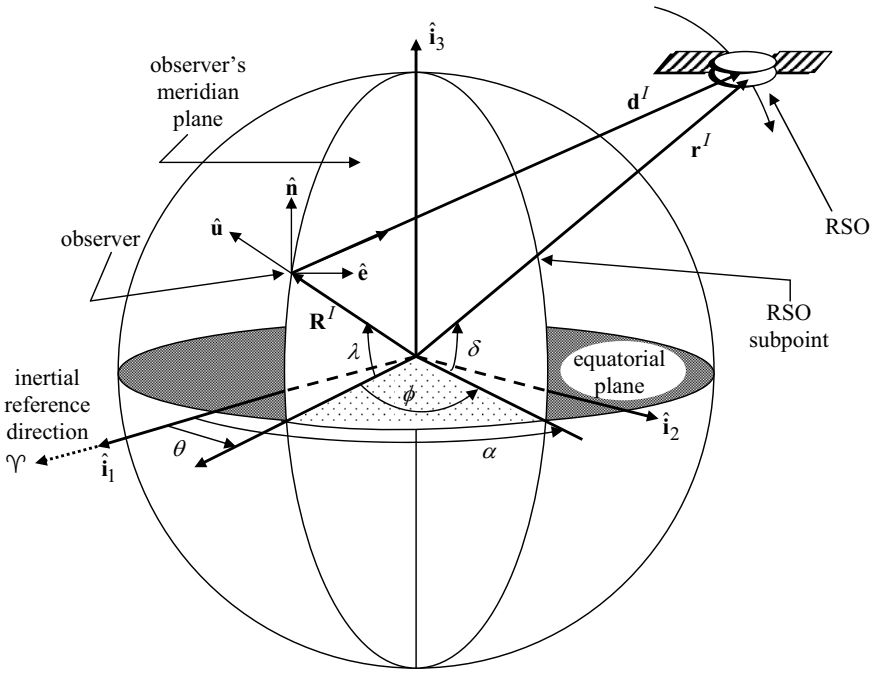

Figure 2. Geometry of Earth Observations of RSO Motion

IV. Observation Models

A. Astrometric Observation Model

This work considers observations made by a optical site which measures the topocentric azimuth and elevation to an RSO. The geometry and common terminology associated with this observation is shown in Figure 2, where $\mathbf{d}^I$ is the position vector from the observer to the RSO, $\mathbf{r}^I$ is the position of the RSO in inertial coordinates, $\mathbf{R}^I$ is the radius vector locating the observer, α and δ are the geocentric right ascension and declination of the RSO, respectively, θ is the sidereal time of the observer, λ is the geodetic latitude of the observer, and ϕ is the east longitude from the observer to the RSO. The basis vectors $\{\hat{\mathbf{i}}_1,\ \hat{\mathbf{i}}_2,\ \hat{\mathbf{i}}_3\}$ are the axis of the inertial coordinate system. The fundamental observation is given by

$$\mathbf{d}^I = \mathbf{r}^I - \mathbf{R}^I \tag{11}$$

In non-rotating equatorial (inertial) components the vector $\mathbf{d}^I$ is given by

$$\mathbf{d}^I = \begin{bmatrix} x - ||\mathbf{R}^I|| \cos(\theta)\cos(\lambda) \\ y - ||\mathbf{R}^I|| \sin(\theta)\cos(\lambda) \\ z - ||\mathbf{R}^I|| \sin(\lambda) \end{bmatrix} \tag{12}$$

The conversion from the inertial to the observer coordinate system (Up-East-North) is given by

$$\begin{bmatrix} \rho_u \\ \rho_e \\ \rho_n \end{bmatrix} = \begin{bmatrix} \cos(\lambda) & 0 & \sin(\lambda) \\ 0 & 1 & 0 \\ -\sin(\lambda) & 0 & \cos(\lambda) \end{bmatrix} \begin{bmatrix} \cos(\theta) & \sin(\theta) & 0 \\ -\sin(\theta) & \cos(\theta) & 0 \\ 0 & 0 & 1 \end{bmatrix} \mathbf{d}^I \tag{13}$$

The angle observations consist of the azimuth, az, and elevation, el. The observation equations are given by

$$\text{az} = \text{atan2}\left(\rho_e,\ \rho_n\right) \tag{14a}$$

$$\text{el} = \sin^{-1}\left(\frac{\rho_u}{\|\mathbf{d}^I\|}\right) \tag{14b}$$

where atan2 is the four-quadrant arctangent function.

B. Light Curve Observation Model

While observing to the azimuth and elevation, the optical site also records the magnitude of the brightness of the RSO. The brightness of an object in space can be modeled using an anisotropic Phong light diffusion model.[21] This model is based on the bidirectional reflectance distribution function (BRDF) which models light distribution scattered from the surface due to the incident light. The BRDF at any point on the surface is a function of two directions, the direction from which the light source originates and the direction from which the scattered light leaves the observed the surface. The model in Ref. 21 decomposes the BRDF into a specular component and a diffuse component. The two terms sum to give the total BRDF:

$$\rho_{\text{total}}(i) = \rho_{\text{spec}}(i) + \rho_{\text{diff}}(i) \tag{15}$$

The diffuse component represents light that is scattered equally in all directions (Lambertian) and the specular component represents light that is concentrated about some direction (mirror-like). Reference 21 develops a model for continuous arbitrary surfaces but simplifies for flat surfaces. This simplified model is employed in this work as shape models are considered to consist of a finite number of flat facets. Therefore the total observed brightness of an object becomes the sum of the contribution from each facet.

Under the flat facet assumption the specular term of the BRDF becomes[21]

$$\rho_{\text{spec}}(i) = \frac{\sqrt{(n_u+1)\,(n_v+1)}}{8\pi} \frac{\left(\mathbf{u}_n^I(i)\cdot\mathbf{u}_h^I\right)^{n_u(\mathbf{u}_h^I\cdot\mathbf{u}_u^I(i))^2+n_v(1-(\mathbf{u}_h^I\cdot\mathbf{u}_u^I(i))^2)}}{\mathbf{u}_n^I(i)\cdot\mathbf{u}_{\text{sun}}^I + \mathbf{u}_n^I(i)\cdot\mathbf{u}_{\text{obs}}^I - (\mathbf{u}_n^I(i)\cdot\mathbf{u}_{\text{sun}}^I)(\mathbf{u}_n^I(i)\cdot\mathbf{u}_{\text{obs}}^I)} F_{\text{reflect}}(i) \tag{16}$$

where the Fresnel reflectance is given by

$$F_{\text{reflect}}(i) = R_{\text{spec}}(i) + (1 - R_{\text{spec}}(i)) \left(1 - \mathbf{u}^I_{\text{sun}} \cdot \mathbf{u}^I_h(i)\right)^5 \tag{17}$$

The parameters n_u and n_v are terms of the Phong model which are used to weight directionality of specularly reflected light off some materials (e.g. copper). The terms in Eq. (16) are functions of the reflection geometry which is described in Figure 1. The diffuse term of the BRDF is

$$\rho_{\text{diff}}(i) = \left(\frac{28 R_{\text{diff}}(i)}{23\pi}\right)(1 - R_{\text{spec}}(i)) \left[1 - \left(1 - \frac{\mathbf{u}^I_n(i) \cdot \mathbf{u}^I_{\text{sun}}}{2}\right)^5\right] \left[1 - \left(1 - \frac{\mathbf{u}^I_n(i) \cdot \mathbf{u}^I_{\text{obs}}}{2}\right)^5\right] \tag{18}$$

The apparent magnitude of an RSO is the result of sunlight reflecting off of its surfaces along the line-of-sight to an observer. First, the fraction of visible sunlight that strikes each facet of the RSO (and not absorbed) is computed by

$$F_{\text{sun}}(i) = C_{\text{sun,vis}}\, \rho_{\text{total}}(i) \left(\mathbf{u}^I_n(i) \cdot \mathbf{u}^I_{\text{sun}}\right) \tag{19}$$

where $C_{\text{sun,vis}} = 455$ W/m^2 is the power per square meter impinging on a particular facet due to visible light striking the surface. If either the angle between the surface normal and the observer's direction or the angle between the surface normal and Sun direction is greater than $\pi/2$ then there is no light reflected toward the observer. If this is the case then the fraction of visible light is set to $F_{\text{sun}}(i) = 0$. Next, the fraction of sunlight that strikes facet i which is reflected must be computed:

$$F_{\text{obs}}(i) = \frac{F_{\text{sun}}(i)\mathcal{A}(i) \left(\mathbf{u}^I_n(i) \cdot \mathbf{u}^I_{\text{obs}}\right)}{\|\mathbf{d}^I\|^2} \tag{20}$$

The reflected light is now used to compute the apparent brightness magnitude, which is measured by an observer:

$$m_{\text{app}} = -26.7 - 2.5\log_{10}\left|\sum_{i=1}^{N} \frac{F_{\text{obs}}(i)}{C_{\text{sun,vis}}}\right| \tag{21}$$

where -26.7 is the apparent magnitude of the sun.

V. Unscented Filtering Using Light Curve Data

The Unscented Kalman filter (UKF) is chosen for state estimation because it has at least the accuracy of a second-order filter[15] without the requirement of computing Jacobians like

the extended Kalman filter. The UKF is used to estimate the rotational and translational states based on fusing angles and light curve data along with their associated models as discussed in Section III. The global parameterization of the attitude in the UKF is the quaternion while a minimal parameterization involving the generalized Rodrigues parameters (GRPs) is used to define the local error.[22] Quaternions are the global parameterization of choice because their kinematics are free of singularities. The representation of the attitude error as a GRP is useful for the propagation and update stages of the attitude covariance because the structure of the UKF can be used directly. Complete explanations of the quaternion and its mapping to GRPs are provided in Refs. 18 and 23. The angles data can be used to determine the unknown position and velocity of an RSO, but if the position is coupled with the attitude dynamics then angles data can assist with attitude estimation as well. However, if position is known accurately, then using only light curve data is sufficient to estimate the shape with the MMAE process.

A UKF estimating the position ($\mathbf{r}^I$), velocity ($\mathbf{v}^I$), attitude ($\mathbf{q}_I^B$) and rotation rate ($\boldsymbol{\omega}_{B/I}^B$) of an RSO is now summarized. Equations (2) and (7) can be expressed in general as

$$\dot{\mathbf{x}} = \mathbf{f}\left(\mathbf{x}, t\right) + G\left(\mathbf{x}, t\right)\boldsymbol{\Gamma}(t) \tag{22}$$

where $\mathbf{x}$ is the state of the system, $\boldsymbol{\Gamma}(t)$ is a Gaussian white-noise process term with covariance $Q\delta(t_1 - t_2)$. The function $\mathbf{f}\left(\mathbf{x}, t\right)$ is the nonlinear dynamics and $G(\mathbf{x}, t)$ is the model error distribution matrix. To solve the general nonlinear filtering problem the UKF utilizes the unscented transformation to determine the mean and covariance propagation though the function $\mathbf{f}\left(\mathbf{x}, t\right)$. If the initial pdf $p(\mathbf{x}_0)$ is given, the solution for the time evolution of the conditional pdf, $p(\mathbf{x}, t|\tilde{\mathbf{Y}})$ constitutes the nonlinear filtering problem. Here $\tilde{\mathbf{Y}}$ is the sequence of all available measurements up to the current time.

Given a system model with initial state and covariance values, the UKF propagates the state vector and the error-covariance matrix recursively. At discrete observation times, the UKF updates the state and covariance matrix conditioned on the information gained by the latest measurement. Discrete measurements are assumed to have the following form:

$$\tilde{\mathbf{y}}_k = \mathbf{h}\left(\mathbf{x}_k, t_k\right) + \mathbf{v}_k \tag{23}$$

where $\tilde{\mathbf{y}}_k$ is a measurement vector and $\mathbf{v}_k$ is the measurement noise, which is assumed to be a zero-mean Gaussian random variable with covariance $R_k\delta_{jk}$.

The UKF operates under the principle that (i) it is easier to propagate samples from a pdf through a general nonlinear function than to propagate the pdf itself and (ii) Gaussian distributions can be represented by a finite set of deterministically selected samples known as sigma points. Given an $L \times L$ error-covariance matrix P_k, the $2L + 1$ sigma points are

constructed by

$$\boldsymbol{\sigma}_k \leftarrow 2L \text{ columns from } \pm\sqrt{(L+\lambda)P_k} \tag{24a}$$

$$\boldsymbol{\chi}_k(0) = \boldsymbol{\mu}_k \tag{24b}$$

$$\boldsymbol{\chi}_k(i) = \boldsymbol{\sigma}_k(i) + \boldsymbol{\mu}_k \tag{24c}$$

where $\sqrt{M}$ is shorthand notation for a matrix Z such that $M = Z\,Z^T$ and $\boldsymbol{\mu}_k$ is the mean of the distribution. Given that these points are selected to represent the distribution of the state vector, each sigma point is given a weight that preserves the information contained in the initial distribution:

$$W_0^{\text{mean}} = \frac{\lambda}{L+\lambda} \tag{25a}$$

$$W_0^{\text{cov}} = \frac{\lambda}{L+\lambda} + (1-\alpha^2+\beta) \tag{25b}$$

$$W_i^{\text{mean}} = W_i^{\text{cov}} = \frac{1}{2(L+\lambda)}, \quad i = 1,\, 2,\, \ldots,\, 2L \tag{25c}$$

where $\lambda = \alpha^2(L+\kappa) - L$ is a composite scaling parameter. The constant α controls the spread of the sigma point distribution and should be a small number $0 < \alpha \leq 1$, κ provides an extra degree of freedom that is used to fine-tune the higher-order moments, and β is used to incorporate prior knowledge of the distribution by weighting the mean sigma point in the covariance calculation. Typically $\beta = 2$ and $\kappa = 3 - L$ are good starting guesses for tuning the filter.

The reduced state vector for the joint attitude and position estimation problem is given by

$$\hat{\mathbf{x}}_k^- = \left.\begin{bmatrix} \boldsymbol{\delta}\hat{\mathbf{p}}^- \\ \hat{\boldsymbol{\omega}}^- \\ \hat{\mathbf{r}}^{I-} \\ \hat{\mathbf{v}}^{I-} \end{bmatrix}\right|_{t_k} \tag{26}$$

where $\boldsymbol{\delta}\hat{\mathbf{p}}$ is the error GRP states associated with the quaternion $\hat{\mathbf{q}}_I^B$ and $\hat{\cdot}$ is used to denote an estimate. Here it is noted that the subscript B/I and superscript B in $\boldsymbol{\omega}_{B/I}^B$ are omitted in this and the following sections for clarity. The initial estimate $\hat{\mathbf{x}}_0$ is the mean sigma point and is denoted $\boldsymbol{\chi}_0(0)$. The error GRP state of the initial estimate is set to zero, while the rest of the states are initialized by their respective initial estimates.

A. Predictor

The attitude state errors are represented as error GRPs resulting in a minimum parameter representation for the attitude state error.[22] To within first order, the state error covariance of the attitude is invariant whether the errors are parameterized using quaternions or GRPs.[24] Therefore the attitude state error-covariance can be directly decomposed into error GRP sigma points for use in the UKF. The sigma points corresponding to the error GRPs are first converted into error quaternions so that the quaternion sigma points can be computed. The error quaternion, denoted by $\boldsymbol{\delta}\mathbf{q}_k^-(i)$, associated with the i^{th} error GRP sigma point is computed by[22]

$$\boldsymbol{\delta}\boldsymbol{\varrho}_k^-(i) = f^{-1}\left[a + \delta q_{4_k}^-(i)\right]\boldsymbol{\chi}_k^{\delta p}(i) \tag{27a}$$

$$\delta q_{4_k}^-(i) = \frac{-a||\boldsymbol{\chi}_k^{\delta p}(i)||^2 + f\sqrt{f^2 + (1-a^2)||\boldsymbol{\chi}_k^{\delta p}(i)||^2}}{f^2 + ||\boldsymbol{\chi}_k^{\delta p}(i)||^2} \tag{27b}$$

$$\boldsymbol{\delta}\mathbf{q}_k^-(i) = \begin{bmatrix}\boldsymbol{\delta}\boldsymbol{\varrho}_k^-(i)\\ \delta q_{4_k}^-(i)\end{bmatrix} \tag{27c}$$

where a is a parameter from 0 to 1 and f is a scale factor, which is often set to $f = 2(a+1)$ so that the attitude error covariance is that of the small roll, pitch and yaw angle errors. Here it is noted that the subscript I and superscript B in $\mathbf{q}_I^B$ and its estimates are omitted in this and the following sections for clarity. The i^{th} quaternion sigma point is given by a rotation of $\boldsymbol{\delta}\mathbf{q}_k^-(i)$ about the *a priori* estimate:

$$\hat{\mathbf{q}}_k^-(i) = \boldsymbol{\delta}\mathbf{q}_k^-(i) \otimes \hat{\mathbf{q}}_k^-(0) \tag{28}$$

where

$$\mathbf{q}' \otimes \mathbf{q} \equiv \begin{bmatrix}\Psi(\mathbf{q}') & \mathbf{q}'\end{bmatrix}\mathbf{q} \tag{29}$$

The sigma points are propagated through the system dynamics:

$$\dot{\boldsymbol{\chi}}(i) = \mathbf{f}\left(\boldsymbol{\chi}(i), \hat{\mathbf{q}}(i)\right) \tag{30}$$

where

$$\mathbf{f}\left(\boldsymbol{\chi}, \hat{\mathbf{q}}\right) = \begin{bmatrix} \frac{1}{2}\Xi(\hat{\mathbf{q}})\hat{\boldsymbol{\omega}} \\ J_{\text{RSO}}^{-1}\left(\hat{\mathbf{T}}_{\text{srp}}^B - [\hat{\boldsymbol{\omega}}\times]\, J_{\text{RSO}}\hat{\boldsymbol{\omega}}\right) \\ \hat{\mathbf{v}}^I \\ -\frac{\mu}{\hat{r}^3}\hat{\mathbf{r}}^I + \hat{\mathbf{a}}_{J_2} + \hat{\mathbf{a}}_{\text{SRP}}^I \end{bmatrix} \tag{31}$$

The estimated acceleration and torque due to SRP are calculated with Eqs. (8) and (10), respectively. After propagation, the sigma points for the error GRP states are computed with the propagated attitude sigma points. The estimated mean sigma point quaternion, $\hat{\mathbf{q}}^-_{k+1}(0)$, is stored, and error quaternions corresponding to each propagated quaternion sigma point are computed as:

$$\boldsymbol{\delta}\hat{\mathbf{q}}^-_{k+1}(i) = \hat{\mathbf{q}}^-_{k+1}(i) \otimes \left[\hat{\mathbf{q}}^-_{k+1}(0)\right]^{-1} \tag{32}$$

where the notation for the conjugate quaternion is defined as:

$$\mathbf{q}^{-1} \equiv \begin{bmatrix} -\boldsymbol{\varrho} \\ q_4 \end{bmatrix} \tag{33}$$

Using the result of Eq. (32), the error GRP sigma points are computed as

$$\boldsymbol{\delta}\mathbf{p}^-_{k+1}(i) = f\frac{\boldsymbol{\delta}\hat{\boldsymbol{\varrho}}^-_{k+1}(i)}{a + \delta\hat{q}^-_{4_{k+1}}(i)} \tag{34}$$

After setting the error GRP for the mean sigma point to zero, the propagated sigma points are reconstructed as in Eq. (26) The propagated mean and covariance are calculated as a weighted sum of the sigma points as

$$\hat{\mathbf{x}}^-_{k+1} = \sum_{i=0}^{2L} W_i^{\text{mean}}\, \boldsymbol{\chi}_{k+1}(i) \tag{35a}$$

$$P^-_{k+1} = \sum_{i=0}^{2L} W_i^{\text{cov}} \left[\boldsymbol{\chi}_{k+1}(i) - \hat{\mathbf{x}}^-_{k+1}\right]\left[\boldsymbol{\chi}_{k+1}(i) - \hat{\mathbf{x}}^-_{k+1}\right]^T + Q_{k+1} \tag{35b}$$

where Q_{k+1} is the discrete-time process noise covariance.

B. Corrector

As previously discussed, measurements are available in the form of azimuth, elevation and apparent brightness magnitude, $\tilde{\mathbf{y}} \equiv [\tilde{m}_{\text{app}} \quad \tilde{\text{az}} \quad \tilde{\text{el}}]^T$. Estimated observations are computed for each sigma point using the observation models discussed in Section IV:

$$\boldsymbol{\gamma}_k(i) = \mathbf{h}\left[\boldsymbol{\chi}_k(i), \hat{\mathbf{q}}^-_k(i)\right] \tag{36}$$

The mean estimated output is then computed as

$$\hat{\mathbf{y}}^-_k = \sum_{i=0}^{2L} W_i^{\text{mean}}\, \boldsymbol{\gamma}_k(i) \tag{37}$$

The output, innovations and cross-correlation covariance are computed as

$$P_k^{yy} = \sum_{i=0}^{2L} W_i^{\text{cov}} \left[\boldsymbol{\gamma}_k(i) - \hat{\mathbf{y}}_k^-\right] \left[\boldsymbol{\gamma}_k(i) - \hat{\mathbf{y}}_k^-\right]^T \tag{38a}$$

$$P_k^{\upsilon\upsilon} = P_k^{yy} + R_k \tag{38b}$$

$$P_k^{xy} = \sum_{i=0}^{2L} W_i^{\text{cov}} \left[\boldsymbol{\chi}_k(i) - \hat{\mathbf{x}}_k^-\right] \left[\boldsymbol{\gamma}_k(i) - \hat{\mathbf{y}}_k^-\right]^T \tag{38c}$$

The gain is given by

$$K_k = P_k^{xy} (P_k^{\upsilon\upsilon})^{-1} \tag{39}$$

The UKF update equations are given by

$$\hat{\mathbf{x}}_k^+ = \hat{\mathbf{x}}_k^- + K_k \left[\tilde{\mathbf{y}}_k - \hat{\mathbf{y}}_k^-\right] \tag{40a}$$

$$P_k^+ = P_k^- - K_k P_k^{\upsilon\upsilon} K_k^T \tag{40b}$$

The quaternion update is performed by converting the error GRP states of $\hat{\mathbf{x}}_k^+$ to a quaternion, $\boldsymbol{\delta}\hat{\mathbf{q}}_k^+$, via Eq. (27), and performing

$$\hat{\mathbf{q}}_k^+ = \boldsymbol{\delta}\hat{\mathbf{q}}_k^+ \otimes \hat{\mathbf{q}}_k^-(0) \tag{41}$$

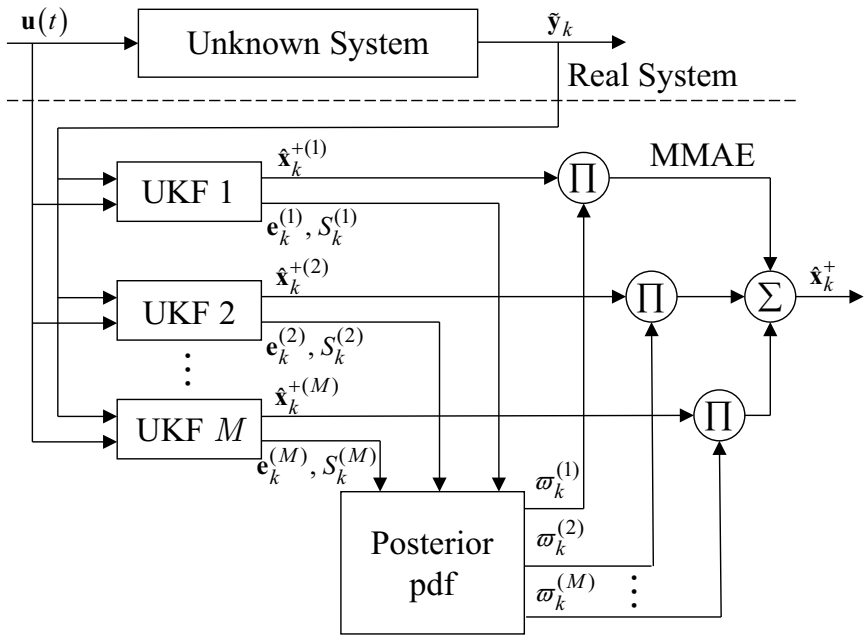

Figure 3. MMAE Process

VI. Multiple-Model Adaptive Estimation

This section provides a brief review of the multiple-model adaptive estimation algorithm. More details can be found in Refs. 25 and 26. Multiple-model adaptive estimation (MMAE) is a recursive algorithm that uses a bank of estimators, each dependent on a particular hypothesis, to determine an estimate based upon an unknown physical process under consideration. In particular, the hypotheses can correspond to different mathematical models of the same physical process, or of the same model but dependent upon different constants or model parameters. The basic framework of MMAE can be seen in Figure 3.

A. MMAE Weights

A finite set of hypothesis $\{\mathbf{p}^{(\ell)};\, \ell = 1, \ldots, M\}$ are used to seed the bank of estimators. The finite set of parameters can be the results of discretizing a continuous parameters space or describe a discrete parameter space of interest. The goal of the estimation process is to determine the conditional pdf of the ℓ^{th} hypothesis, $\mathbf{p}^{(\ell)}$, given all the measurements. Application of Bayes' rule yields

$$p\left(\mathbf{p}^{(\ell)}|\tilde{\mathbf{Y}}_k\right) = \frac{p\left(\tilde{\mathbf{Y}}_k|\mathbf{p}^{(\ell)}\right) p\left(\mathbf{p}^{(\ell)}\right)}{\sum_{j=1}^{M} p\left(\tilde{\mathbf{Y}}_k|\mathbf{p}^{(j)}\right) p\left(\mathbf{p}^{(j)}\right)} \tag{42}$$

where $\tilde{\mathbf{Y}}_k$ denotes the sequence $\{\tilde{\mathbf{y}}_0, \tilde{\mathbf{y}}_1, \ldots, \tilde{\mathbf{y}}_k\}$. The *a posteriori* probabilities can be computed through[27]

$$\begin{aligned} p\left(\mathbf{p}^{(\ell)}|\tilde{\mathbf{Y}}_k\right) &= \frac{p\left(\tilde{\mathbf{y}}_k,\, \mathbf{p}^{(\ell)}|\tilde{\mathbf{Y}}_{k-1}\right)}{p\left(\tilde{\mathbf{y}}_k|\tilde{\mathbf{Y}}_{k-1}\right)} \\ &= \frac{p\left(\tilde{\mathbf{y}}_k|\hat{\mathbf{x}}_k^{-(\ell)}\right) p\left(\mathbf{p}^{(\ell)}|\tilde{\mathbf{Y}}_{k-1}\right)}{\sum_{j=1}^{M}\left[p\left(\tilde{\mathbf{Y}}_k|\hat{\mathbf{x}}_k^{-(j)}\right) p\left(\mathbf{p}^{(j)}|\tilde{\mathbf{Y}}_{k-1}\right)\right]} \end{aligned} \tag{43}$$

The conditional probabilities of the observations based on each hypothesis (likelihood), $p\left(\tilde{\mathbf{y}}_k|\hat{\mathbf{x}}_k^{-(\ell)}\right)$, are given as

$$p\left(\tilde{\mathbf{y}}_k|\hat{\mathbf{x}}_k^{-(\ell)}\right) = \frac{1}{\det\left(2\pi S_k^{(\ell)}\right)^{1/2}} \exp\left\{-\frac{1}{2}\mathbf{e}_k^{(\ell)T} {S_k^{(\ell)}}^{-1} \mathbf{e}_k^{(\ell)}\right\} \tag{44}$$

where measurement residual for the ℓ^{th} hypothesis is given by

$$\mathbf{e}_k^{(\ell)} = \tilde{\mathbf{y}}_k - \hat{\mathbf{y}}_k^{-(\ell)} \tag{45}$$

and corresponding residual covariance matrix from the UKF is

$$S_k^{(\ell)} = P_k^{vv} \tag{46}$$

where P_k^{vv} is given by Eq. (38b) using the ℓ^{th} filter.

Note that the denominator of Eq. (43) is just a normalizing factor to ensure that $p\left(\mathbf{p}^{(\ell)}|\tilde{\mathbf{Y}}_k\right)$ is a pdf. Equation (43) can now be recast as a recursion formula to define the MMAE weights $\varpi_k^{(\ell)}$ as

$$\begin{aligned} \varpi_k^{(\ell)} &= \varpi_{k-1}^{(\ell)} p\left(\tilde{\mathbf{y}}_{k-1}|\hat{\mathbf{x}}_{k-1}^{-(\ell)}\right) \\ \varpi_k^{(\ell)} &\leftarrow \frac{\varpi_k^{(\ell)}}{\sum_{j=1}^{M} \varpi_k^{(j)}} \end{aligned} \tag{47}$$

where $\varpi_k^{(\ell)} \equiv p\left(\mathbf{p}^{(\ell)}|\tilde{\mathbf{y}}_k\right)$. Note that only the current time likelihood function is needed to update the weights. The weights at time t_0 are initialized to $\varpi_0^{(\ell)} = 1/M \ \forall \ \ell$. The convergence properties of MMAE are shown in Ref. 27, which assumes ergodicity in the proof. The ergodicity assumptions can be relaxed to asymptotic stationarity and other assumptions are even possible for non-stationary situations.[28]

From Eq. (47) and Eq. (44) it is seen that hypotheses having lower residuals will have probabilities that will increase with time; this will favor hypotheses that fit the observations better. Also from Eq. (44) it is seen that hypotheses which have small values for $\det(S_k^{(\ell)})$ will have probabilities that will grow. Assuming that all filters have same measurement noise covariance matrix R_k, this will favor hypotheses that have smaller variance. Therefore the MMAE process will tend to select the minimum variance hypothesis from the set of hypotheses.

B. Fusion of MMAE Estimates

In addition to assigning a conditional probability to a given hypothesis, MMAE can, in some instances, provide a fused state estimate, associated error covariance and hypothesis. This is typically accomplished by means of a weighted average of each filters *a posteriori* estimate. However, this fusion is only applicable when fusion of the individual filters state estimate or hypothesis yield physically meaningful results. Such is the case in Ref. 29 where MMAE

is used to estimate the process noise covariance for a given dynamical system. For other MMAE applications, such as three-axis gyro calibration,[30] the hypotheses under consideration correspond to different mathematical models of the gyro which lead each filter to have its own unique state vector. For this application, the notion of a fused hypothesis or state vector does not have any tractable meaning. Thus Ref. 30 selects the hypothesis with the highest weight, ϖ, to be the best representative MMAE estimate.

In this work a combination approach is taken. The hypotheses for the MMAE are different candidate shape models for an RSO, yet each filter estimates a common state vector. Because the shape models cannot be fused to have physical meaning, the shape model having the highest weight is accepted as being the MMAE estimated shape. Since the state vector is common to all of the filters, a representative MMAE state estimate can be formed using a weighted average of each filters *a posteriori* state estimates.

Traditionally, the conditional mean given an MMAE approach uses a weighted sum of each of the filter estimates as shown in Figure 3:

$$\hat{\mathbf{x}}_k^+ = \sum_{\ell=1}^{M} \varpi_k^{(\ell)} \hat{\mathbf{x}}_k^{+(\ell)} \tag{48}$$

However, in this work because the state vectors contain quaternion estimates an additive approach to determining the conditional mean will, in general, yield an improper quaternion which violates the unit norm constraint. Rather, a two-step process is used to determine the conditional mean and covariance. This process begins by defining a reference attitude, $\bar{\mathbf{q}}_k$, from which all of the quaternion estimates are referenced. The weighted average quaternion from the set of all *a posteriori* quaternion estimates is selected as the reference attitude. The average quaternion is the normalized eigenvector corresponding to the maximum eigenvalue of the matrix[31]

$$\mathcal{M} = -\sum_{\ell=1}^{M} \varpi_k^{(\ell)} \Xi\left(\hat{\mathbf{q}}_k^{+(\ell)}\right) P_{\boldsymbol{\alpha}\boldsymbol{\alpha}}^{+(\ell)^{-1}} \Xi^T\left(\hat{\mathbf{q}}_k^{+(\ell)}\right) \tag{49}$$

where $P_{\boldsymbol{\alpha}\boldsymbol{\alpha}}^{+(\ell)}$ is the 3×3 portion of the covariance corresponding to the attitude estimates. Once the reference attitude is determined, the attitude correction associated with estimate from the ℓ^{th} filter is determined as

$$\boldsymbol{\delta}\mathbf{q}_k^{+(\ell)} = \hat{\mathbf{q}}_k^{+(\ell)} \otimes \bar{\mathbf{q}}_k^{-1} \tag{50}$$

which is converted into the corresponding GRP correction, $\boldsymbol{\delta}\mathbf{p}_k^{+(\ell)}$, with Eq. (34). After

defining $\bar{\mathbf{x}}_k^{+(\ell)^T} \equiv [\boldsymbol{\delta}\mathbf{p}_k^{+(\ell)^T} \quad \hat{\boldsymbol{\omega}}_k^{+(\ell)^T} \quad \hat{\mathbf{r}}_k^{I+(\ell)^T} \quad \hat{\mathbf{v}}_k^{I+(\ell)^T}]$, the following is computed:

$$\bar{\mathbf{x}}_k^+ = \sum_{\ell=1}^{M} \varpi_k^{(\ell)} \bar{\mathbf{x}}_k^{+(\ell)} \tag{51}$$

The conditional mean is then given by

$$\hat{\mathbf{x}}_k^+ = \begin{bmatrix} \hat{\mathbf{q}}_k^+ \\ \hat{\boldsymbol{\omega}}_k^+ \\ \hat{\mathbf{r}}_k^{I+} \\ \hat{\mathbf{v}}_k^{I+} \end{bmatrix} \tag{52}$$

where the conditional mean quaternion is given by $\hat{\mathbf{q}}_k^+ = \boldsymbol{\delta}\mathbf{q}_k^+ \otimes \bar{\mathbf{q}}_k^+$ and $\boldsymbol{\delta}\mathbf{q}_k^+$ is the quaternion formed from $\boldsymbol{\delta}\mathbf{p}_k^+$, the first three components of $\bar{\mathbf{x}}_k^+$. This approach is essentially the same as used within the UKF presented in Section V for the fusion of sigma points which contain a quaternion. With this approach, the conditional covariance can be calculated as

$$P_k^+ = \sum_{\ell=1}^{M} \varpi_k^{(\ell)} \left(P_k^{+(\ell)} + \left[\bar{\mathbf{x}}_k^{+(\ell)} - \bar{\mathbf{x}}_k^+ \right] \left[\bar{\mathbf{x}}_k^{+(\ell)} - \bar{\mathbf{x}}_k^+ \right]^T \right) \tag{53}$$

VII. Simulation Results

Two simulation scenarios are presented to show the performance of the MMAE approach to estimate the shape of an RSO from magnitude and angles observations. For both scenarios, an RSO is in near geosynchronous orbit with orbital elements given by $a = 42,364.17$ km, $e = 2.429 \times 10^{-4}$, $i = 30$ deg, $\omega = \Omega = 0.0$ deg and $M_0 = 91.065$ deg. The simulation epoch is 15-March-2010 at 04:00:00 GST. The initial quaternion and angular rate of the RSO are given by $\mathbf{q}_I^B \equiv [0.7041 \;\; 0.0199 \;\; 0.0896 \;\; 0.7041]^T$ and $\boldsymbol{\omega}_{B/I}^B = [206.26 \;\; 103.13 \;\; 540.41]^T$ deg/hr.

Brightness magnitude and angle observations are simulated using a ground station located at 20.71° North, 156.26° West longitude and 3,058.6 m altitude. Measurements constructed using instantaneous geometry are corrupted by zero-mean Gaussian white noise with standard deviations of 1 arc-seconds on the azimuth observation, 1 arc-seconds on the elevation observation and 0.1 for the brightness magnitude.[4] Observations are available every 5 seconds for one hour.

The convergence of the UKF used within the MMAE approach is studied using a Monte Carlo simulation. Reference 22 discusses the limitations of the UKF approach implemented in this paper in terms of approximating the attitude error. This, along with the nonlinearity of the measurement model, limits the convergence radius of the UKF. Therefore, the covariance

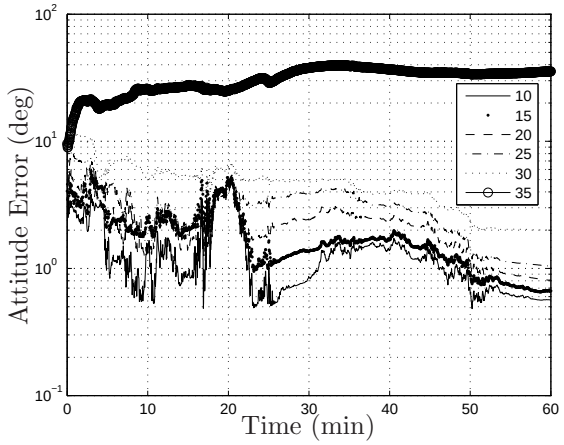

Figure 4. Attitude Error Monte Carlo Simulation

matrix of the attitude parameters is limited in size to allow for proper convergence. This convergence radius is determined from Monte Carlo simulations. The results from these simulations are shown in Figure 4. These simulations consist of UKFs that are all initialized with the same covariance for all states except the attitude states. Initial estimates are randomly sampled from a Gaussian distribution with a mean equal to the true state vector and covariance values equal to the UKF's initialized values. The 3σ values for angular rates, position, and velocity are taken to be 72 deg/hr, 300 km and 3 km/s, respectively. The attitude 3σ values are varied from 10 deg to 35 deg in 5 deg increments. For each value 1,000 Monte Carlo simulations are performed. Then for each individual simulation the root-mean-square error is determined and averaged over all 1,000 simulations for a given 3σ value. From Figure 4 it can be seen that the UKF shows good convergence performance for 3σ values up to 30 deg. This work uses 20 deg for the attitude 3σ value but this can be extended to be a covering of attitude states as long as each component has a 3σ value less than approximately 30 deg.

RSO shape models are randomly generated and can be generically grouped into two categories: regular polygon prisms and rectangular cuboids. The regular polygon prisms are prisms whose ends (i.e. top and bottom) are regular shapes. The regular polygon prisms are then further divided into equilateral triangular prisms, square prisms and regular hexagonal prisms. The shape of a regular polygon prism is defined by the number of sides n, side length s and height h. Examples of the three regular polygon prisms considered with body axis descriptions can be found in Figure 5(a). Assuming constant density throughout the shape

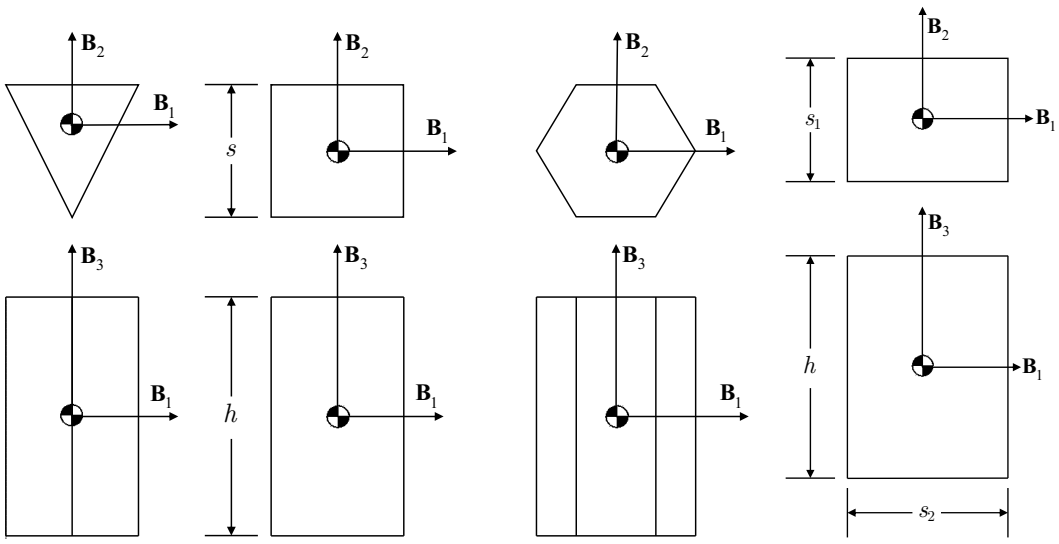

(a) Regular Polygon Prism

(b) Rectangular Cuboid

Figure 5. RSO Shape Model Geometry

model, the moment of inertia matrices for each of the regular polygon models are given by

$$J_{\text{triangle}} = m_{\text{RSO}} \begin{bmatrix} \frac{s^2}{24} + \frac{h^2}{12} & 0 & 0 \\ 0 & \frac{s^2}{24} + \frac{h^2}{12} & 0 \\ 0 & 0 & \frac{s^2}{12} \end{bmatrix} \tag{54a}$$

$$J_{\text{square}} = m_{\text{RSO}} \begin{bmatrix} \frac{s^2}{12} + \frac{h^2}{12} & 0 & 0 \\ 0 & \frac{s^2}{12} + \frac{h^2}{12} & 0 \\ 0 & 0 & \frac{s^2}{6} \end{bmatrix} \tag{54b}$$

$$J_{\text{hexagon}} = m_{\text{RSO}} \begin{bmatrix} \frac{5s^2}{24} + \frac{h^2}{12} & 0 & 0 \\ 0 & \frac{5s^2}{24} + \frac{h^2}{12} & 0 \\ 0 & 0 & \frac{5s^2}{24} \end{bmatrix} \tag{54c}$$

The rectangular cuboids are prisms defined by two side lengths s_1 and s_2 as well as the height h, shown in Figure 5(b). The moment of inertia matrix for the cuboids is given by

$$J_{\text{cuboid}} = \frac{m_{\text{RSO}}}{12} \begin{bmatrix} s_2^2 + h^2 & 0 & 0 \\ 0 & s_1^2 + h^2 & 0 \\ 0 & 0 & s_1^2 + s_2^2 \end{bmatrix} \tag{55}$$

Table 1. Polygon Prism Shape Model Parameters

Model	n ()	s (m)	h (m)	Model	n ()	s (m)	h (m)
1	3	2.7894	0.7826	14	4	3.7868	3.8503
2	4	1.3222	0.7281	15	6	3.0139	1.1782
3	4	3.4060	3.0337	16	6	4.2873	3.7044
4	4	1.1759	1.2799	17	6	4.9415	3.4672
5	4	2.2876	1.6275	18	4	4.6481	4.1222
6	3	1.9290	2.0149	19	4	2.0535	4.1416
7	6	2.6976	2.0378	20	6	0.0117	1.4739
8	4	4.9586	1.9371	21	3	2.7090	1.5538
9	4	3.7785	3.0529	22	6	1.0466	2.6199
10	4	4.9025	0.8428	23	4	1.1042	1.6332
11	4	1.1816	0.9486	24	3	1.6358	4.1609
12	3	2.6475	0.4822	25	4	0.4888	4.0534
13	4	0.2667	1.6227				

Fifty models (25 regular polygon prisms and 25 cuboids) are randomly generated by sampling side lengths and heights from a uniform distribution on the interval $[0.01, 5]$ m. For the regular polygon prisms, the number of sides are also selected randomly on the interval $[3, 6]$, with all instances of 5 sides being set to 4 as pentagonal prism models are not included. The models are shown in Table 1 and 2. In addition to the model geometry, the material properties are also defined such that for each model, all facets are assumed to have the following: $R_{\text{spec}} = 0.7$, $R_{\text{diff}} = 0.3$, $\epsilon = 0.5$. The Phong parameters n_u and n_v are each taken to be equal to 1,000 for all facets of every model. Each shape model is assumed to have a mass of 1,000 kg.

The first simulation is used as a baseline to show how the proposed MMAE approach can identify the shape of an unknown RSO when the exact RSO shape model exists within the set of hypothesized shape models. The 50 models shown in Table 1 and 2 are used as the model bank. From this bank, a single model is chosen to act as the true model for the simulation. The initial states for each filter are given by $\hat{\mathbf{q}}_I^B(t_0) = [0.7500 \quad 0.0712 \quad 0.0947 \quad 0.6508]^T$ (a 10 degree attitude error), $\hat{\boldsymbol{\omega}}_{B/I}^B(t_0) = [220.26 \quad 117.13 \quad 554.41]^T$, $\hat{a}(t_0) = 42,364.148255$ km, $\hat{e}(t_0) = 2.4290 \times 10^{-4}$, $\hat{i}(t_0) = 30.0083$ deg, $\hat{\omega}(t_0) = -1.172$ deg, $\hat{\Omega}(t_0) = 0.0$ deg and $\hat{M}_0(t_0) = 92.137$ deg. Initial 3σ values are taken to be 20 deg for the attitude states, 72 (deg/hr) on the angular rates, 300 km on position and 3 (km/s) on velocity. The process noise for the UKFs are taken as $Q_k^{(\ell)} = 0$ for this proof of concept simulation.

In this case the true model is a hexagonal prism ($n = 6$) with $s = 1.0466$ m and $h = 2.6199$

Table 2. Cubiod Shape Model Parameters

Model	s_1 (m)	s_2 (m)	h (m)	Model	s_1 (m)	s_2 (m)	h (m)
1	2.1858	1.5339	0.3966	14	1.0762	4.3117	3.7319
2	2.1000	1.5000	0.3800	15	1.9952	3.0776	0.6364
3	1.4426	3.8187	2.7211	16	1.6750	4.9560	4.1137
4	4.6382	4.1340	1.6973	17	1.1557	1.0265	0.1355
5	0.2661	2.8716	4.1633	18	4.6812	4.1378	2.0780
6	2.9674	3.9650	2.7673	19	3.4191	3.3825	3.6597
7	0.8229	1.6519	4.7881	20	4.8109	1.2523	3.9091
8	4.1936	1.1251	4.4652	21	2.1955	2.3842	1.8428
9	0.8461	1.5688	1.7890	22	4.7023	2.0014	3.7269
10	2.5160	2.9268	2.7365	23	0.0391	3.0012	4.4624
11	4.9967	4.1513	1.7399	24	3.0554	4.0046	1.2206
12	1.7835	1.4594	3.1178	25	4.0074	0.5343	0.6567
13	0.2449	2.0187	3.9852				

m. The time history of the MMAE weight for this simulation can be found in Figure 7. As seen from this figure, the MMAE algorithm is able to converge to the true shape model model with no ambiguity. The state errors and respective 3σ bounds are shown in Figure 8. The position and velocity errors are plotted in radial (R), in-track (IT), and cross-track (CT) or RIC coordinates. The transformation from inertial to RIC coordinates is given by

$$A_I^{\text{ric}} = \begin{bmatrix} \mathbf{n}_r^T & \mathbf{n}_i^T & \mathbf{n}_c^T \end{bmatrix} \tag{56}$$

where $\mathbf{n}_r = \mathbf{r}^I/\|\mathbf{r}^I\|$ is the radial direction, $\mathbf{n}_i = [\mathbf{n}_c\times]\mathbf{n}_r/\|[\mathbf{n}_c\times]\mathbf{n}_r\|$ is the in-track direction, and $\mathbf{n}_c = [\mathbf{r}^I\times]\mathbf{v}^I/\|[\mathbf{r}^I\times]\mathbf{v}^I\|$ is the cross-track direction. The errors associated with the attitude and angular rate states are very large for approximately the first 10 minutes of the simulation until they converge rapidly to their, effectively, steady-state values. Referring back to Figure 7, it is seen that this convergence is coincident with the convergence of the MMAE algorithm. Figure 8 also provides some qualitative insight into the observability of the estimated states. The fact that there is such a large change in the conditional error indicates that the attitude and angular rate states are highly dependent upon the shape model. This is in contrast to the position and velocity states which are only very weakly coupled to the shape via the SRP induced drag.

To determine the benefit of blending the attitude states verses choosing the best attitude estimate a Monte Carlo simulation is conducted. The blended attitude states are determined

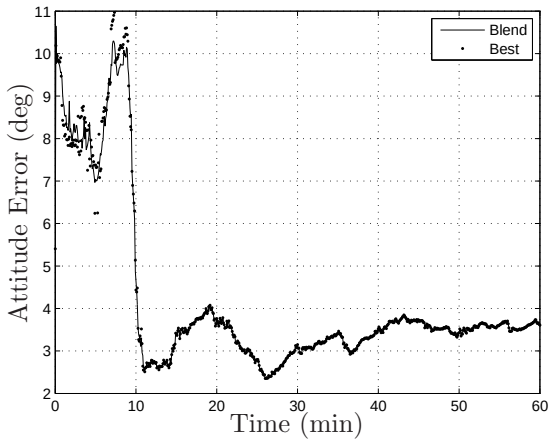

Figure 6. Blending vs. Best Estimate Monte Carlo Simulation

using the quaternion averaging approach discussed previously and the best attitude estimate is determined by the model with the largest probability. This simulation uses the same initial condition and uncertainties as scenario one and a 1,000 random samples are selected from the initial uncertainties. For each sample the MMAE approach is simulated for scenario one and both the blended attitude states and best attitude estimates are determined. Then the error is averaged over all 1,000 samples. The results are shown in Figure 6. From this figure it can be seen that the difference between the two approaches isn't very large but the blended estimates do provide smaller error. As the MMAE approach converges to a model in the bank both approaches result in the same error.

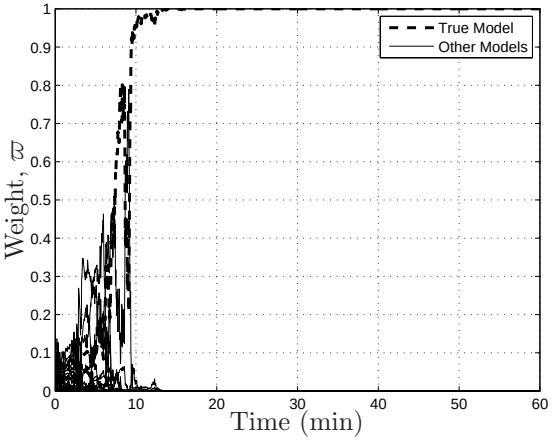

Figure 7. MMAE Weights for Simulation 1

For the second simulation, the true shape model is not within the bank of models. For

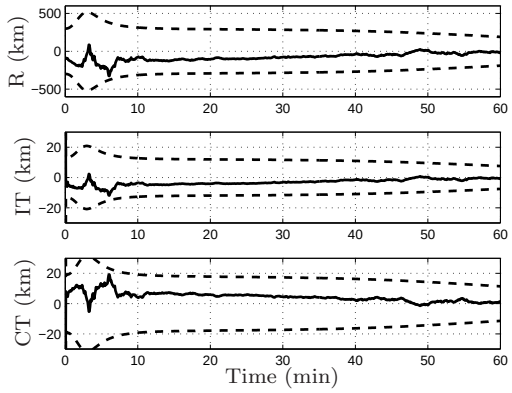

(a) Position Errors

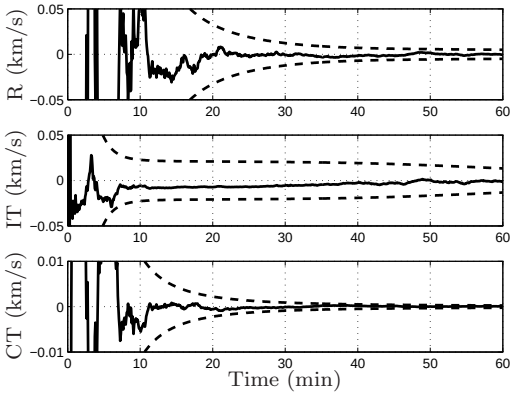

(b) Velocity Errors

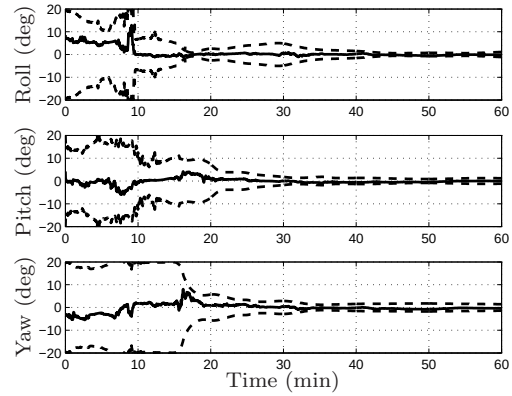

(c) Attitude Errors

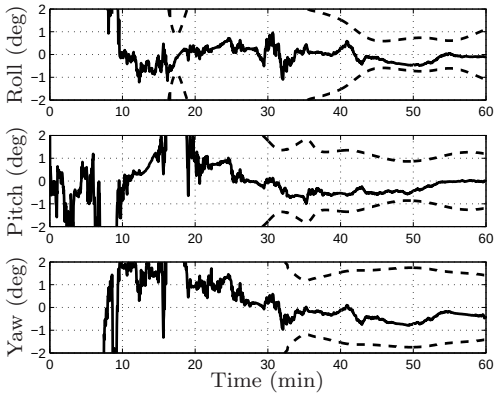

(d) Attitude Errors (zoomed)

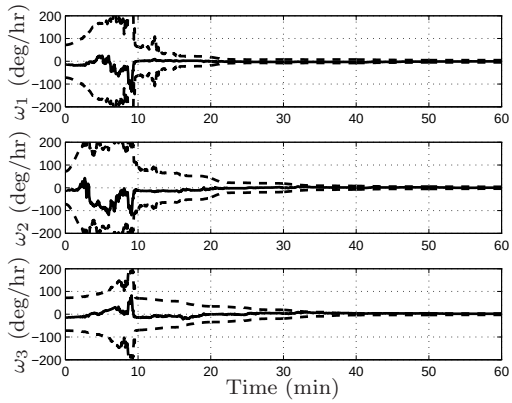

(e) Angular Rates

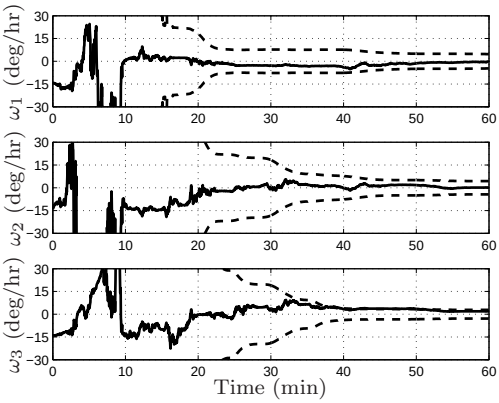

(f) Angular Rates (zoomed)

Figure 8. Simulation 1 State Errors and 3σ Bounds

this case the true shape model is selected as a rectangular cuboid with sides $s_1 = 2.0$ m, $s_2 = 1.5$ m and $h = 0.375$ m. The bank of 50 shape models, initial state estimates and covariance values are the same as in the first simulation. The MMAE weights can be found in Figure 9. In this case the MMAE weights for two models are nonzero. These models represent the closest approximation to the true model that the bank of models holds. The models with nonzero weights are both rectangular cuboids with dimensions $s_1 = 2.1858$ m, $s_2 = 1.5339$ m and $h = 0.3966$ m (Close Model 1, which corresponds to Model 1 in Table 2) and $s_1 = 2.1000$ m, $s_2 = 1.5000$ m and $h = 0.3800$ m (Close Model 2, which corresponds to Model 2 in Table 2). The shape model estimate is chosen to be the model with the highest probability and therefore switches between Model 1 and Model 2 over the simulation period as these models contend for the highest probability. While the dimensions are not exact with the true model, the principal result is that the MMAE algorithm is able to identify the form of the RSO shape; in this case a plate-like shape with one dimension much smaller than the other two. This information could be further used to redefine the model bank in order to find a better shape model estimate or for classifying a piece of debris (e.g. such as a sheared off solar panel), but is considered outside of the scope of the current work.

The estimated errors and associated 3σ bounds are shown in Figure 10. The position and velocity estimates do not suffer from the lack of knowledge of the true shape model. However, the accuracy of the attitude and angular rate states are degraded because of the uncertainty in the shape model. In particular, the errors in the rotational states are about three-times larger for this simulation compared to the previous simulation case.

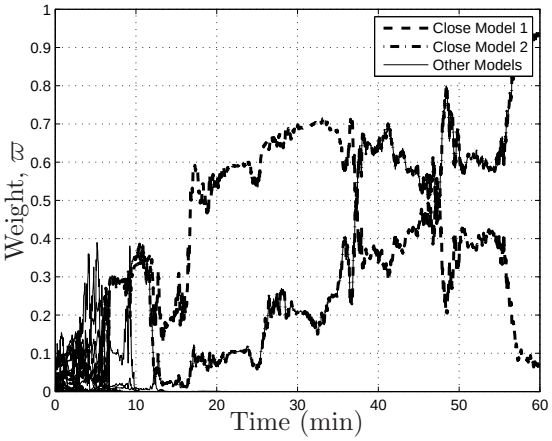

Figure 9. MMAE Weights for Simulation 2

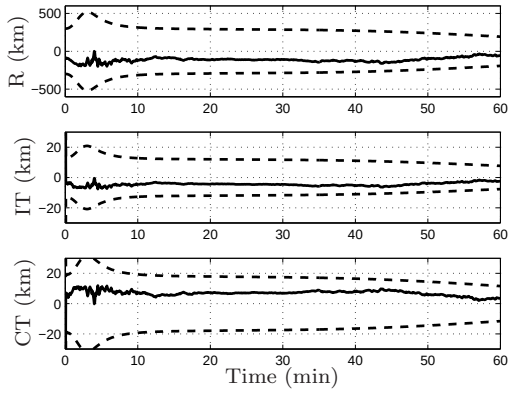

(a) Position Errors

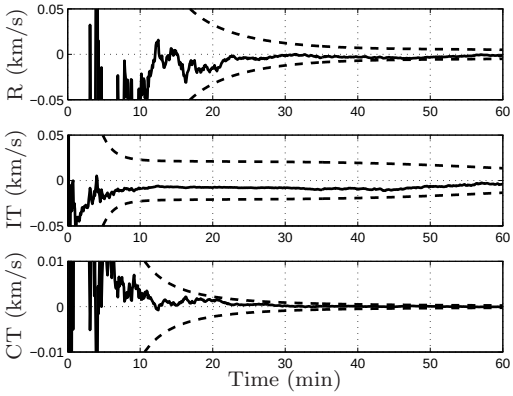

(b) Velocity Errors

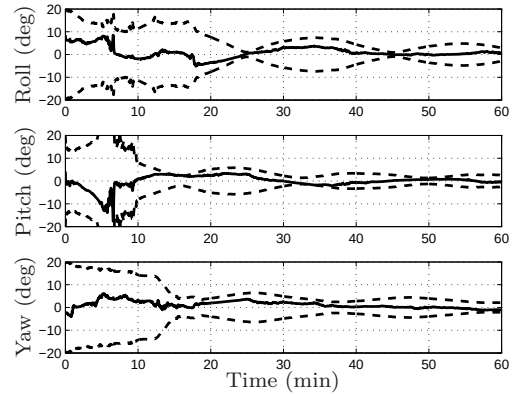

(c) Attitude Errors

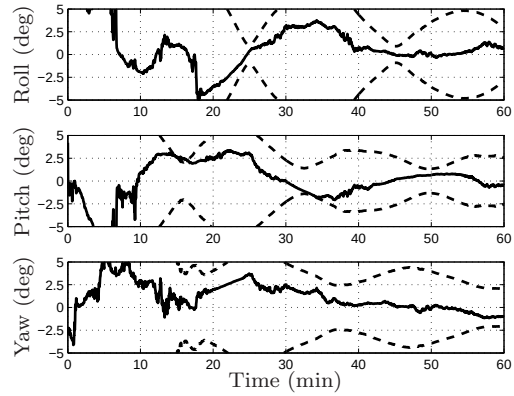

(d) Attitude Errors (zoomed)

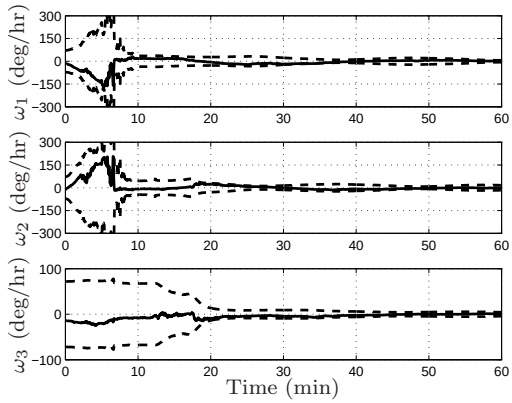

(e) Angular Rates

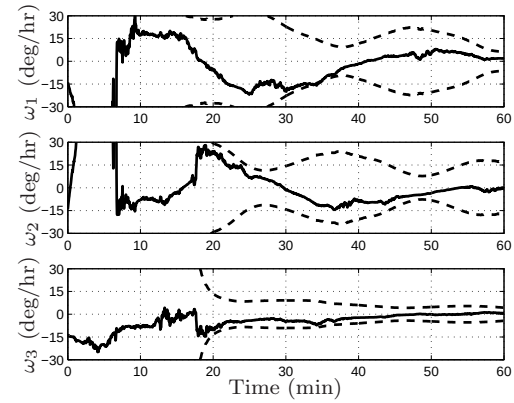

(f) Angular Rates (zoomed)

Figure 10. Simulation 2 State Errors and 3σ Bounds

VIII. Conclusion

In this paper a multiple-model adaptive estimation algorithm using light curve and angles data was presented. This was used to identify the most probable shape of an unknown resident space object along with its associated rotational and translational states. The algorithm exploits passively collected data, meaning that only the data currently used in the tracking of resident space objects is necessary. This is an operationally important feature of the algorithm because no new sensors or specific tasking is necessary. Initial simulation results show that when the true shape model is within the bank of models considered, the algorithm is able to select the correct model without any ambiguity. When the true shape model is not within the bank, the algorithm is able to determine which shape model(s) contained within the bank best approximates the unknown shape. Also, the attitude estimate converges when the initial attitude is known with 30 degrees (3σ) of the true attitude. These results show that the presented multiple-model adaptive estimation approach can be beneficial for the tracking and characterization of resident space objects.

IX. Acknowledgement

This work was supported through multiple funding mechanisms, one of which was via the Air Force Research Laboratory, Space Vehicles Directorate (ASTRIA and Space Scholars program). The authors wish to thank Frank J. Centinello III for his work with Dr. Moriba Jah to further the research in light curve and angles data fusion.

References

[1]Sato, T., Wakayama, T., Tanaka, T., Ikeda, K.-i., and Kimura, I., "Shape of Space Debris as Estimated from Radar Cross Section Variations," *Journal of Spacecraft and Rockets*, Vol. 31, No. 4, July-Aug. 1994, pp. 665–670.

[2]Walker, J.L., "Range-Doppler Imaging of Rotating Objects," *IEEE Transactions on Aerospace and Electronics Systems*, Vol. AES-16, No. 4, Jan. 1980, pp. 23–52.

[3]Hagfors, T., "Mapping Planetary Surfaces by Radar," *Proceedings of the IEEE*, Vol. 61, No. 9, Jan. 1973, pp. 1219–1225.

[4]Hall, D.T., Africano, J.L., Lambert, J.V., and Kervin, P.W., "Time-Resolved I-Band Photometry of Calibration Spheres and NaK Droplets," *Journal of Spacecraft and Rockets*, Vol. 44, No. 4, July 2007, pp. 910–919.

[5]DiMatteo, J., Florakis, D., Weichbrod, A., and Milam, M., "Proximity Operations Testing with a Rotating and Translating Resident Space Object," *AIAA Guidance, Navigation and Control Conference*, Chicago, IL, Aug. 2009, AIAA-2009-6293.

[6]Lichter, M.D. and Dubowsky, S., "State, Shape, and Parameter Estimation of Space Objects from

Range Images," *Proceedings of the 2004 IEEE International Conference on Robotics & Automation*, New Orleans, LA, April 2004, pp. 2974–2979.

[7]Young, G.S.J. and Chellappa, R., "3-D Motion Estimation using a Sequence of Noisy Stereo Images: Models, Estimation, and Uniqueness Results," *IEEE Transactions on Pattern Analysis and Machine Intelligance*, Vol. 12, No. 8, Aug. 1990, pp. 735–759.

[8]Broida, T.J. and Chellappa, R., "Estimating the Kinematics and Structure of a Rigid Object from a Sequence of Monocular Images," *IEEE Transactions on Pattern Analysis and Machine Intelligence*, Vol. 13, No. 6, June 1991, pp. 497–513.

[9]Kaasalainen, M. and Torppa, J., "Optimization Methods for Asteriod Lightcurve Inversion I: Shape Determination," *Icarus*, Vol. 153, No. 4, Jan. 2001, pp. 24–36.

[10]Kaasalainen, M. and Torppa, J., "Optimization Methods for Asteriod Lightcurve Inversion II: The Complete Inverse Problem," *Icarus*, Vol. 153, No. 4, Jan. 2001, pp. 37–51.

[11]Calef, B., Africano, J., Birge, B., Hall, D., and Kervin, P., "Photometric Signature Inversion," *Proceedings of the International Society for Optical Engineering*, Vol. 6307, San Diego, CA, Aug. 2006, Paper 11.

[12]Jah, M. and Madler, R., "Satellite Characterization: Angles and Light Curve Data Fusion for Spacecraft State and Parameter Estimation," *Proceedings of the Advanced Maui Optical and Space Surveillance Technologies Conference*, Vol. 49, Wailea, Maui, HI, Sept. 2007, Paper E49.

[13]Centinello, F.J., "Six Degree of Freedom Estimation with Light Curve Data," Tech. rep., Air Force Research Laboratory, Kihei, HI, 2008.

[14]Jazwinski, A.H., *Stochastic Processes and Filtering Theory*, chap. 8, Academic Press, San Diego, CA, 1970.

[15]Julier, S.J., Uhlmann, J.K., and Durrant-Whyte, H.F., "A New Method for the Nonlinear Transformation of Means and Covariances in Filters and Estimators," *IEEE Transactions on Automatic Control*, Vol. AC-45, No. 3, March 2000, pp. 477–482.

[16]Gordon, N.J., Salmond, D.J., and Smith, A.F.M., "Novel Approach to Nonlinear/Non-Gaussian Bayesian State Estimation," *IEE Proceedings, Part F - Communications, Radar and Signal Processing*, Vol. 140, No. 2, Seattle, WA, April 1993, pp. 107–113.

[17]Wetterer, C.J. and Jah, M., "Attitude Estimation from Light Curves," *Journal of Guidance, Control and Dynamics*, Vol. 32, No. 5, Sept.-Oct. 2009, pp. 1648–1651.

[18]Shuster, M.D., "A Survey of Attitude Representations," *Journal of the Astronautical Sciences*, Vol. 41, No. 4, Oct.-Dec. 1993, pp. 439–517.

[19]Borderies, N. and Longaretti, P., "A New Treatment of the Albedo Radiation Pressure in the Case of a Uniform Albedo and of a Spherical Satellite," *Celestial Mechanics and Dynamical Astronomy*, Vol. 49, No. 1, March 1990, pp. 69–98.

[20]Vallado, D.A., *Fundamentals of Astrodynamics and Applications*, McGraw-Hill, New York, NY, 3rd ed., 1997, pp. 574–578.

[21]Ashikmin, M. and Shirley, P., "An Anisotropic Phong Light Reflection Model," Tech. Rep. UUCS-00-014, University of Utah, Salt Lake City, UT, 2000.

[22]Crassidis, J.L. and Markley, F.L., "Unscented Filtering for Spacecraft Attitude Estimation," *Journal of Guidance, Control and Dynamics*, Vol. 26, No. 4, July-Aug. 2003, pp. 536–542.

[23]Schaub, H. and Junkins, J.L., "Stereographic Orientation Parameters for Attitude Dynamics: A Generalization of the Rodrigues Parameters," *Journal of the Astronautical Sciences*, Vol. 44, No. 1, Jan.-March 1996, pp. 1–20.

[24]Markley, F.L., "Attitude Error Representations for Kalman Filtering," *AIAA Journal of Guidance, Control, and Dynamics*, Vol. 26, No. 2, March-April 2003, pp. 311–317.

[25]Brown, R.G. and Hwang, P.Y.C., *Introduction to Random Signals and Applied Kalman Filtering*, John Wiley & Sons, New York, NY, 3rd ed., 1997, pp. 353–361.

[26]Stengel, R.F., *Optimal Control and Estimation*, Dover Publications, New York, NY, 1994, pp. 402–407.

[27]Anderson, B.D.O. and Moore, J.B., *Optimal Filtering*, chap. 10.1, Dover Publications, Mineola, NY, 2005.

[28]Anderson, B.D.O., Moore, J.B., and Hawkes, R.M., "Model Approximations via Prediction Error Identification," *Automatica*, Vol. 14, No. 6, Nov. 1978, pp. 615–622.

[29]Alsuwaidan, B.N., Crassidis, J.L., and Cheng, Y., "Generalized Multiple Model Adaptive Estimation Using an Autocorrelation Approach," *IEEE Transactions on Aerospace and Electronic Systems*, Vol. 47, No. 3, July 2011, pp. 2138–2151.

[30]Lam, Q.M. and Crassidis, J.L., "Evaluation of a Multiple Model Adaptive Estimation Scheme for Space Vehicle's Enhanced Navigation Solution," *AIAA Guidance, Navigation and Control Conference*, Hilton Head, SC, Aug. 2007, AIAA-07-6816.

[31]Markley, F.L., Crassidis, J.L., Oshman, Y., and Cheng, Y., "Averaging Quaternions," *AIAA Journal of Guidance, Control, and Dynamics*, Vol. 30, No. 4, July-Aug. 2007, pp. 1193–1197.